ARCHIVE OF MECHANICAL ENGINEERING

DOI: 10.24425/ame.2022.141517 2022, Vol. 69, No. 3, pp. 541–565

Van Luc NGUYEN [1], Duy Khanh HO [1]

Numerical investigation of vortex wake patterns of laminar flow around two side-by-side cylinders

Received 9 March 2022, **Revised** 3 June 2022, **Accepted** 7 June 2022, **Published online** 10 September 2022

Keywords: viscous fluid, vortex shedding, vortex wake pattern, vortex-in-cell method, two side-by-side cylinders

The laminar flow around two side-by-side circular cylinders was numerically investigated using a vortex-in-cell method combined with a continuous-forcing immersed boundary method. The Reynolds number (Re) of the flow was examined in the range from 40 to 200, and the distance between the cylinders varies from $1.2D$ to $6D$, where D is the cylinder diameter. Simulation results show that the vortex wake is classified into eight patterns, such as single-bluff-body, meandering-motion, steady, deflected-in-one-direction, flip-flopping, anti-phase-synchronization, in-phase-synchronization, and phase-difference-synchronization, significantly depending on the Re, the cylinder distance, and the initial external disturbance effects. The anti-phase-synchronization, in-phase-synchronization, and phase-difference-synchronization vortex patterns can be switched at a low Re after a long time evolution of the flow. In particular, the single-bluff-body and flip-flopping vortex patterns excite the oscillation amplitude of the drag and lift coefficients exerted on the cylinders.

1. Introduction

The problem of flows around two cylinders in a side-by-side arrangement is widely observed in various engineering applications, such as heat exchangers, oil platforms, and chemical plants. Characteristics of this flow type are vortex sheddings, interaction between the vortex wakes downstream, and the fluid forces acting on the cylinders. A comprehensive understanding of these flow phenomena is essential in designing and controlling the related high-efficiency devices. This

✉ Corresponding author, Email: vlnguyen@tdmu.edu.vn

[1] Institute of Engineering and Technology, Thu Dau Mot University, Binh Duong Province, Vietnam. ORCID (V.L.N): 0000-0001-8746-3646

has attracted the attention of many experimental and numerical researchers over several decades.

Ishigai et al. [1] experimentally investigated the interaction of the Karman vortex streets of flow generated from two cylinders at the Reynolds numbers (Re) in the range from 1500 to 15000. The behavior of vortices shed from both cylinders with their distance of $L \geqslant 2D$ is the same as that of the flow around a single cylinder, where D is the cylinder diameter. When the distance is small, the shear layers separated from cylinders deflect to the right and the left equally because of the Coanda effects. The vortex shedding frequencies of two cylinders differ, and wakes shed from these cylinders combine into a pair of the Karman vortex streets. Bearman and Wadcock [2] experimentally examined the flow around two side-by-side cylinders at $\mathrm{Re} = 2.5 \times 10^4$ and showed a mean repulsive force between the cylinders in proximity. At a small distance, the drags of cylinders in flow interference are less than their sum in an isolation state. Vortices are shed from both cylinders and form two vortex streets when the distance is larger than one diameter. When the cylinders nearly touch, the vortices are alternatively shed from their sides and only form one vortex street. Zdravkovich [3] classified the flow interference regimes into a single vortex street with a small cylinder distance, bistable flow with a critical distance, and synchronization in phase of two parallel streets with a larger distance. Williamson [4] experimentally examined the mechanism of the wakes of the flow passing two cylinders at Re = 55, 100 and 200 and found three flow regimes. When the distance varies from $L = 2D$ to $6D$, the wake is composed of two parallel streets in-phase or anti-phase. The anti-phase pattern is stable, and the shape of vortices is conserved downstream far from the cylinders. For the in-phase pattern, vortex streets are only stable in regions near the cylinders. The vortices far from the cylinders combine to form large-scale ones. Kim and Durbin [5] experimentally investigated an unsteady wake at the cylinder distance less than one diameter at $\mathrm{Re} = 2 \div 7 \times 10^3$. They found that the wakes behave in flip-flopping motion between two asymmetric states without a natural period. The time-scale for the flip-flopping phenomena is several orders of magnitude longer than vortex shedding from each cylinder.

The investigations of the flow around two side-by-side cylinders have also been performed using numerical simulations [6–10]. Chang and Song [6] analyzed the flow at Re = 100 and observed the bistable nature of the asymmetric vortex shedding and an intermittent change from one status to another between symmetric and anti-symmetric wake patterns. Kang [7] further found deflected and steady wake patterns at Re in the range from 40 to 160. Other numerical investigations [8–10], based on finite-element and finite-volume methods, also reported the above flow characteristics. These investigations mostly focused on validating numerical methods to simulate a complex flow around multiple bodies rather than clarifying the flow wake mechanism. This study will shed some light on this topic and offers a comprehensive understanding of the mechanism of vortex wake pattern of flow around two side-by-side cylinders using a Vortex-In-Cell (VIC) method.

The cylinder distance is varied from $1.2D$ to $6D$, and the Re examined ranges from 40 to 200. Moreover, the flow under the external disturbance effects in a short period of its evolution is, for the first time, investigated to explore the potential vortex patterns.

The VIC method was introduced by Birdsall and Fuss [11] to simulate two-dimensional plasma problems. It was then adapted to simulate the two-dimensional incompressible inviscid fluid flow by Christiansen [12]. Cottet and Koumoutsakos [13] combined it with a viscous model to simulate two- and three-dimensional incompressible viscous flows. A VIC method was developed to simulate the flow around two tandem cylinders, the flow around four cylinders of various shapes, and the vortex–wall interaction by Nguyen et al. [14–16]. It was proven that the method could capture the vortex shedding, the interaction between the vortex wakes, the fluid forces exerted on the cylinders, and the vortex formation and deformation due to the wall effects. In this study, the VIC method [14, 16] is employed to investigate the characteristics of the laminar flow around two side-by-side cylinders at Re ranging from 40 to 200. The vortex wakes of the flow are identified using the plots of the vorticity contours, and the characteristics of these wakes are analyzed by using plots of the drag and lift coefficients exerted on the cylinders. The rest of the paper is organized as follows: Section 2 describes the governing equations and numerical method, Section 3 offers the discussions on the characteristics of the vortex wake mechanism, and the conclusions are finally given in Section 4.

2. Governing equations and numerical method

2.1. Governing equations

The conservative mass and momentum Navier–Stokes equations for incompressible viscous fluid flow are respectively expressed as follows:

$$\nabla \cdot \boldsymbol{u} = 0, \tag{1}$$

$$\frac{\partial \boldsymbol{u}}{\partial t} + (\boldsymbol{u} \cdot \nabla)\boldsymbol{u} = -\frac{1}{\rho}\nabla p + \nu \nabla^2 \boldsymbol{u} + \boldsymbol{g}, \tag{2}$$

where $\boldsymbol{u}$ is fluid velocity, p is pressure, ν is kinematic viscosity, and $\boldsymbol{g}$ is gravitational acceleration. Taking the curl operation on both sides of Eq. (2), the flow momentum equation is written in the velocity–vorticity form as

$$\frac{\partial \boldsymbol{\omega}}{\partial t} + (\boldsymbol{u} \cdot \nabla)\boldsymbol{\omega} = \nu \nabla^2 \boldsymbol{\omega} + (\boldsymbol{\omega} \cdot \nabla)\boldsymbol{u}, \tag{3}$$

where the vorticity is expressed as $\boldsymbol{\omega} = \nabla \times \boldsymbol{u}$. The second term on the left of Eq. (3) is the vortex convection, expressing the movement of vortices with the conservation of their strength and shape, while the first and second terms on the right are the vortex diffusion and stretching, respectively. The vortex diffusion

describes the diffusion of the vortices owing to the fluid viscosity effects. For two-dimensional problems, the vortex stretching term in Eq. (3) is omitted. Therefore, the momentum equation is rewritten as follows:

$$\frac{\partial \boldsymbol{\omega}}{\partial t} + (\boldsymbol{u} \cdot \nabla)\boldsymbol{\omega} = \nu \nabla^2 \boldsymbol{\omega} \,. \tag{4}$$

Based on the Helmholtz theorem, the flow velocity can be decomposed into irrotational ($\nabla\phi$) and solenoidal ($\nabla \times \boldsymbol{\psi}$) vector fields as

$$\boldsymbol{u} = \nabla\phi + \nabla \times \boldsymbol{\psi} \,, \tag{5}$$

where $\boldsymbol{\psi}$ and ϕ are the vector and scalar potentials of the flow velocity field obtained by solving the Poisson and Laplace equations as

$$\nabla^2 \boldsymbol{\psi} = -\boldsymbol{\omega} \,, \tag{6}$$

$$\nabla^2 \phi = 0 \,. \tag{7}$$

Equations (6) and (7) are derived by taking the curl and divergence operations on both sides of Eq. (5) respectively and using the properties of irrotational and solenoidal vector fields as $\nabla \times (\nabla\phi) = 0$ and $\nabla \cdot \boldsymbol{\psi} = 0$.

2.2. Vortex-in-cell method

The VIC method discretizes the fluid into vortex particles p at positions $\boldsymbol{x}_p$ that move at the speed of $\boldsymbol{u}(\boldsymbol{x}_p)$ by the vortex convection and carry the vorticity field $\boldsymbol{\omega}(\boldsymbol{x}_p)$. The momentum equation, Eq. (4), can be written in the Lagrangian reference frame of vortex particles p transporting the vorticity as

$$\frac{\mathrm{d}\boldsymbol{\omega}(\boldsymbol{x}_p)}{\mathrm{d}t} = \nu \nabla^2 \boldsymbol{\omega}(\boldsymbol{x}_p) \,, \tag{8}$$

$$\frac{\mathrm{d}\boldsymbol{x}_p}{\mathrm{d}t} = \boldsymbol{u}(\boldsymbol{x}_p) \,. \tag{9}$$

The vortex particles are initially distributed on the regular grid nodes, and their vorticity is updated on this grid using Eq. (8) computed using the mesh-based schemes. The particle velocity in Eq. (8) and Eq. (9) is given by the flow velocity at their location. The vortex particles convect to the Lagrangian location by Eq. (9). Subsequently, these particles are redistributed onto the mesh with their vorticity interpolated from the Lagrangian location as

$$\boldsymbol{\omega}(\boldsymbol{x}_q) = \sum_{p}^{N_p} \boldsymbol{\omega}(\boldsymbol{x}_p) W\Big(\frac{x_q - x_p}{\Delta x}\Big) W\Big(\frac{y_q - y_p}{\Delta y}\Big) \,, \tag{10}$$

where $\boldsymbol{x}_q = (x_q, y_q)$ is the coordinate of grid nodes, $\boldsymbol{x}_p = (x_p, y_p)$ is the Lagrangian location, Δx and Δy are grid cell sizes, and N_p is the particle number. $W(x)$ is the third-order accurate interpolation function introduced by Monaghan [17] for smoothed-particle hydrodynamics methods and widely employed by Cottet and Koumoutsakos for vortex methods [13], and it is expressed as

$$W(x) = \begin{cases} 1 - \dfrac{5}{2}|x|^2 + \dfrac{3}{2}|x|^3 & \text{if } |x| \le 1\,, \\ \dfrac{1}{2}(2 - |x|)^2(1 - |x|) & \text{if } 1 < |x| \le 2\,, \\ 0 & \text{if } |x| > 2\,. \end{cases} \tag{11}$$

By using Eq. (11), three first flow momentum $\left[M_0 = \displaystyle\int_V \boldsymbol{\omega}\,\mathrm{d}\boldsymbol{x},\ M_1 = \int_V \boldsymbol{x}\times\boldsymbol{\omega}\,\mathrm{d}\boldsymbol{x},\right.$ and $\left. M_2 = \displaystyle\int_V \boldsymbol{x}\times(\boldsymbol{x}\times\boldsymbol{\omega})\,\mathrm{d}\boldsymbol{x}\right]$ are conserved when interpolating the vorticity field from the Lagrangian locations to the Eulerian grid points and vice versa [18].

2.3. A continuous-forcing immersed boundary method

When the fluid flow passes a solid body, it does not slip on the solid surface. To treat this no-slip condition, Peskin [19] introduced an immersed boundary (IB) method to simulate the complex flow around the solid bodies. This method was then developed over several decades and gained many achievements. Two development branches of the method have been formed as continuous- and discrete-forcing IB methods. When applying the penalization technique (a type of continuous-forcing IB methods) to enforce the no-slip condition of the fluid flow on the solid body surface [16, 20–23], the momentum equation, Eq. (4), is rewritten in the penalization term as

$$\frac{\partial \boldsymbol{\omega}}{\partial t} + (\boldsymbol{u}\cdot\nabla)\boldsymbol{\omega} = \nu\nabla^2\boldsymbol{\omega} + \nabla\times(\lambda\chi_s(\boldsymbol{u}_s - \boldsymbol{u}))\,, \tag{12}$$

where λ is penalization parameter, $\boldsymbol{u}_s$ is solid velocity, and χ_s identifies the solid and fluid regions, $\chi_s(\boldsymbol{x}) = 0$ and 1 if $\boldsymbol{x}$ belongs to the fluid and solid domains, respectively, as shown in Fig. 1. For problem of the flow around multiple solid bodies, χ_s is determined as $\chi_s = \displaystyle\sum_{i=1}^{N_b} \chi_s^i$, where index i indicates ith body and N_b is the number of solid bodies. In the continuous-forcing IB method, the solid domain is also calculated in the simulation procedure. The fluid is mathematically treated as a continuous phase over the solid domain. Therefore, χ_s^i is smoothed near the surface of the ith solid body by using the following Heaviside function [13]:

$$\chi_s^i(d^i) = \begin{cases} 0 & \text{if } d^i < -\varepsilon\,, \\ \dfrac{1}{2}\left[1 + \dfrac{d^i}{\varepsilon} + \dfrac{1}{\pi}\sin\left(\pi\dfrac{d^i}{\varepsilon}\right)\right] & \text{if } |d^i| \leqslant \varepsilon\,, \\ 1 & \text{if } d^i > \varepsilon\,, \end{cases} \tag{13}$$

where d^i is signed distance from the grid node to the ith solid body surface ($d^i > 0$ and $d^i < 0$ if the grid node belongs to solid and fluid domains, respectively, as shown in Fig. 1), $\varepsilon = 2\sqrt{2}\Delta x$, and Δx is the grid cell size. Note that the vorticity and its flux on the solid surfaces are not produced exactly using this penalization technique. However, it can completely capture the flow surrounding the solid body. Based on the splitting method for a partial differential equation, the penalization term from the momentum equation, Eq. (12), can be expressed as

$$\frac{\partial \boldsymbol{u}}{\partial t} = \lambda \chi_s(\boldsymbol{u}_s - \boldsymbol{u})\,. \tag{14}$$

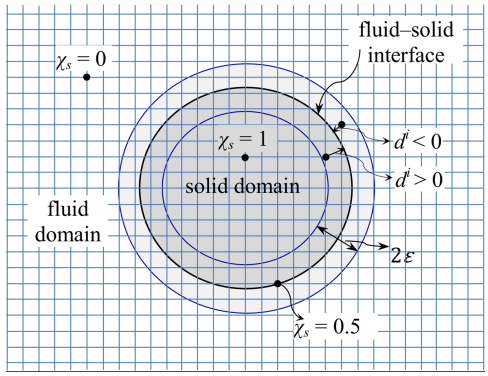

Fig. 1. Schematics of solid, fluid and computational domains, where $\chi_s = 0$, 1 and 0.5 if the grid node belongs to fluid and solid domains and on the fluid–solid interface, respectively. The interface thickness is set as 2ε. d^i is the distance from a grid node to the interface. The value of d^i is positive or negative if a grid node is in the solid or solid domains, respectively

Using the forward finite-difference scheme and setting $\lambda = 1/\Delta t$, the penalization velocity ($\boldsymbol{u}_\lambda$) is calculated as

$$\boldsymbol{u}_\lambda = (1 - \chi_s)\boldsymbol{u} + \chi_s \boldsymbol{u}_s\,, \tag{15}$$

while the penalization vorticity ($\boldsymbol{\omega}_\lambda$) is computed by updating its values implemented using the change in the velocity field as

$$\boldsymbol{\omega}_\lambda = \boldsymbol{\omega} + \nabla \times (\boldsymbol{u}_\lambda - \boldsymbol{u})\,. \tag{16}$$

2.4. Fluid force exerted on the solid body

Given a fluid flow around a circular cylinder at a Re, where $\mathrm{Re} = \rho U_0 D/\mu$, ρ is the fluid density, D is the cylinder diameter, and μ is fluid viscosity, the drag Cd and lift Cl coefficients of the fluid flow exerted on this cylinder are computed as $Cd = (2F_x)/(\rho U_0^2 D_0)$ and $Cl = (2F_y)/(\rho U_0^2 D_0)$. The fluid forces can be estimated as [24]

$$\boldsymbol{F} = -\frac{\mathrm{d}}{\mathrm{d}t}\int_V \boldsymbol{u}d\boldsymbol{x} + \int_\Omega \mathbf{n}\cdot\gamma\,\mathrm{d}\boldsymbol{x}, \tag{17}$$

where $N = 2$ or 3 correspond to two- or three-dimensional flow problems, respectively, V indicates the control volume of the solid body S, Ω is the boundary of this domain, $\mathbf{n}$ is the normal vector of boundary surface Ω, and the flow tensor γ is expressed as

$$\begin{aligned}\gamma =& \frac{1}{2}|\boldsymbol{u}|^2\boldsymbol{I} - \frac{1}{N-1}\boldsymbol{u}\cdot(\boldsymbol{x}\times\boldsymbol{\omega}) + \frac{1}{N-1}\boldsymbol{\omega}\cdot(\boldsymbol{x}\times\boldsymbol{u})\\ &- \frac{1}{N-1}\left[\Big(\boldsymbol{x}\cdot\frac{\partial\boldsymbol{u}}{\partial t}\Big)\boldsymbol{I} - \boldsymbol{x}\cdot\frac{\partial\boldsymbol{u}}{\partial t}\right] + \frac{1}{N-1}[\boldsymbol{x}\cdot(\nabla\cdot\tau)\boldsymbol{I} - \boldsymbol{x}(\nabla\cdot\tau)] + \tau,\end{aligned} \tag{18}$$

where $\boldsymbol{I}$ is unit matrix, and τ is fluid stress tensor defined as $\tau = \mu(\nabla\boldsymbol{u} + \nabla\boldsymbol{u}^T)$. Considering a rectangular control volume of $C_1C_2C_3C_4$ surrounding a cylinder, as sketched in Fig. 2(a), the fluid force components acting on this cylinder are derived as follows [25]:

$$\begin{aligned}F_x =& -\frac{\mathrm{d}}{\mathrm{d}t}\int_V u(1-\chi_S)\,\mathrm{d}x\,\mathrm{d}y\\ &+\int_{C_1}^{C_2}\Big[uv + v\omega y - y\frac{\partial u}{\partial t} + \nu\Big(2\frac{\partial^2 u}{\partial x^2} + \frac{\partial^2 u}{\partial y^2} + \frac{\partial^2 v}{\partial x\partial y}\Big)y - \nu\Big(\frac{\partial u}{\partial y} + \frac{\partial v}{\partial x}\Big)\Big]\,\mathrm{d}x\\ &+\int_{C_2}^{C_3}\Big[\frac{1}{2}(v^2-u^2) - u\omega y - y\frac{\partial v}{\partial t} + \nu\Big(2\frac{\partial^2 v}{\partial y^2} + \frac{\partial^2 v}{\partial x^2} + \frac{\partial^2 u}{\partial x\partial y}\Big)y + 2\nu\Big(\frac{\partial u}{\partial x}\Big)\Big]\,\mathrm{d}y\\ &+\int_{C_3}^{C_4}\Big[-uv - v\omega y + y\frac{\partial u}{\partial t} - \nu\Big(2\frac{\partial^2 u}{\partial x^2} + \frac{\partial^2 u}{\partial y^2} + \frac{\partial^2 v}{\partial x\partial y}\Big)y + \nu\Big(\frac{\partial u}{\partial y} + \frac{\partial v}{\partial x}\Big)\Big]\,\mathrm{d}x\\ &+\int_{C_4}^{C_1}\Big[-\frac{1}{2}(v^2-u^2) + u\omega y + y\frac{\partial v}{\partial t} - \nu\Big(2\frac{\partial^2 v}{\partial y^2} + \frac{\partial^2 v}{\partial x^2} + \frac{\partial^2 u}{\partial x\partial y}\Big)y - 2\nu\Big(\frac{\partial u}{\partial x}\Big)\Big]\,\mathrm{d}y\end{aligned} \tag{19}$$

$$
\begin{aligned}
F_y = &- \frac{\mathrm{d}}{\mathrm{d}t}\int_V v(1-\chi_S)\,\mathrm{d}x\,\mathrm{d}y \\
&+ \int_{C_1}^{C_2}\Big[\frac{1}{2}(v^2-u^2) - v\omega x + x\frac{\partial u}{\partial t} - \nu\Big(2\frac{\partial^2 u}{\partial x^2} + \frac{\partial^2 u}{\partial y^2} + \frac{\partial^2 v}{\partial x \partial y}\Big)x - 2\nu\Big(\frac{\partial v}{\partial y}\Big)\Big]\,\mathrm{d}x \\
&+ \int_{C_2}^{C_3}\Big[-uv + u\omega x + x\frac{\partial v}{\partial t} - \nu\Big(2\frac{\partial^2 v}{\partial y^2} + \frac{\partial^2 v}{\partial x^2} + \frac{\partial^2 u}{\partial x \partial y}\Big)x + \nu\Big(\frac{\partial v}{\partial x} + \frac{\partial u}{\partial y}\Big)\Big]\,\mathrm{d}y \\
&+ \int_{C_3}^{C_4}\Big[-\frac{1}{2}(v^2-u^2) + v\omega x - x\frac{\partial u}{\partial t} + \nu\Big(2\frac{\partial^2 u}{\partial x^2} + \frac{\partial^2 u}{\partial y^2} + \frac{\partial^2 v}{\partial x \partial y}\Big)x + 2\nu\Big(\frac{\partial v}{\partial y}\Big)\Big]\,\mathrm{d}x \\
&+ \int_{C_4}^{C_1}\Big[uv - u\omega x - x\frac{\partial v}{\partial t} + \nu\Big(2\frac{\partial^2 v}{\partial y^2} + \frac{\partial^2 v}{\partial x^2} + \frac{\partial^2 u}{\partial x \partial y}\Big)x - \nu\Big(\frac{\partial v}{\partial x} + \frac{\partial u}{\partial y}\Big)\Big]\,\mathrm{d}y
\end{aligned}
\tag{20}
$$

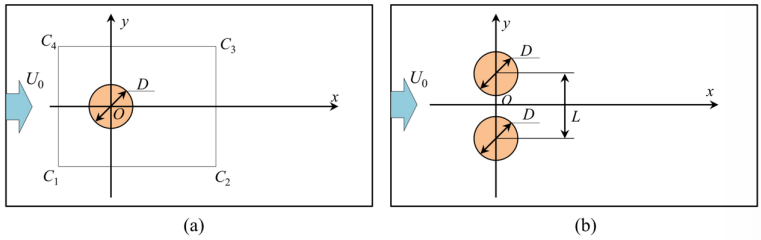

Fig. 2. Schematics of (a) the control volume ($C_1C_2C_3C_4$) employed to calculate the drag (F_x) and lift (F_y) exerted on a cylinder and (b) position of two side-by-side cylinders with their distance L

3. Results and discussions

The present numerical method is verified using simulations of the flow around a single circular cylinder at Re = 200. The computational domain is set as $(-7D, 68D) \times (-7.5D, 7.5D)$ that is divided into square grid cells, and the time step $(U_0\Delta t/(D/2))$ is 0.00125. Nguyen et al. [16] investigated the effects of the domain size and the time step on the simulated results of the flow around two side-by-side cylinders. They pointed out that this domain size and the time step are fine enough to capture the laminar flow characteristics around solid bodies thoroughly. Fig. 3 shows the instantaneous vorticity distribution of the flow around a circular cylinder at Re = 200. The shear layers alternately separated from the

sides of the cylinder roll up to form vortices in opposite rotation directions. These vortices downstream create a vortex wake known as the Karman vortex street. Table 1 shows the time-averaged drag (Cd) and lift (Cl) coefficients and the Strouhal number (St) of the flow around the cylinder at Re = 200 obtained by the current numerical method with various grid resolutions. The Strouhal number is defined as $St = fD/U_0$, where f is the vortex shedding frequency. It is observed that the simulation results are convergent with an increase in the grid resolution. The present results of Cd and Cl have a slight difference from those given by Choi et al. [26] and Harichandan and Roy [27]. However, they agree with those provided by Braza et al. [28] and Supradeepan and Roy [29], and Mimeau et al. [25] well. The Sts obtained by the current numerical method are favorably compared to those from the research works [25–29]. This indicates that the current numerical method can well capture characteristics of laminar flow around bluff bodies.

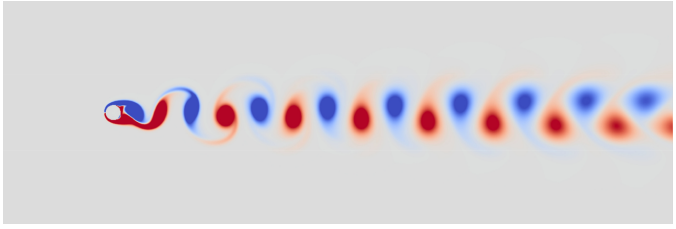

Fig. 3. Instantaneous vorticity distribution of the flow around a single circular cylinders at Re = 200 at $U_0\Delta t/(D/2) = 400$. The vorticity is plotted in the range from −1 to 1, and its positive and negative values are represented in red and blue, respectively

Table 1. Time-averaged drag (Cd) and lift (Cl) coefficients and the Strouhal number (St) of a single circular cylinder immersed in the flow at Re = 200

	Cd	Cl	St
Present ($\Delta x = 0.025$)	1.458±0.05	0±0.73	0.185
Present ($\Delta x = 0.02$)	1.436±0.05	0±0.73	0.19
Present ($\Delta x = 0.01$)	1.42±0.05	0±0.73	0.195
Braza et al. [28]	1.40±0.05	0±0.75	0.19
Choi et al. [26]	1.36±0.048	0±0.64	0.191
Harichandan and Roy [27]	1.32±0.05	0±0.602	0.192
Supradeepan and Roy [29]	1.42±0.05	0±0.652	0.198
Mimeau et al. [25]	1.44±0.05	0±0.75	0.2

In this study, the present numerical method has theoretical order of convergence $p_{\text{theory}} = 2$ in space. However, the boundary condition of the flow on the solid surface reduces this order, and the observed order of convergence will be lower than the theoretical value. To clarify the actual convergence properties, we employ the Richardson extrapolation method to compute the convergence order, as formulated

in detail in appendix A. Three simulations of the flow around two circular cylinders in the side-by-side arrangement, where the grid spacing increases with their ratio of $r = 1.5$, are implemented. The flow conditions for these simulation cases are illustrated in Table 2. From values of the drag coefficient of the upper cylinder (Cd_1), as also listed in Table 2, the convergence order is estimated to be $p = 1.86$. This value demonstrates the consistency of the numerical model developed for solving the problem of the laminar flow around multiple solid bodies. Based on three values of Cd_1, the expected value of Cd_1 at the zero grid spacing ($\Delta x = 0$) in the Richardson extrapolation term (as formulated in appendix A) is obtained as $Cd_{1-\text{expected}} = 1.4$. The values of Cd_1 at four grid resolutions are further described in Fig. 4. It is observed that the Cd_1 at $\Delta x_1 = 0.01D$ is very close to that at $\Delta x = 0$, and the relative error is estimated as 2.7%. Thus, the simulation using the grid spacing of $\Delta x_1 = 0.01D$ can produce reliable results.

Table 2. Simulation conditions of the flow around two side-by-side circular cylinders at the distance of their centers $L = 3D$ at Re = 200 and the drag coefficient of upper cylinder (Cd_1) at $U_0 t/(D/2) = 400$. The time step is set up as $U_0 \Delta t/(D/2) = 0.00125$ for three simulation cases. Three grid spacings have their ratio of $r = 1.5$ ($\Delta x_2 = r\Delta x_1$ and $\Delta x_3 = r\Delta x_2$)

Case	Computational domain	Grid cell number	$\Delta x = \Delta y$	Cd_1
I	$(-7.5D, 22.5D) \times (-7.5D, 7.5D)$	3000×1500	$\Delta x_1 = 0.01D$	1.45185
II	$(-7.5D, 22.5D) \times (-7.5D, 7.5D)$	2000×1000	$\Delta x_2 = 0.015D$	1.53164
III	$(-7.5D, 22.56D) \times (-7.515D, 7.515D)$	1336×668	$\Delta x_3 = 0.0225D$	1.70125

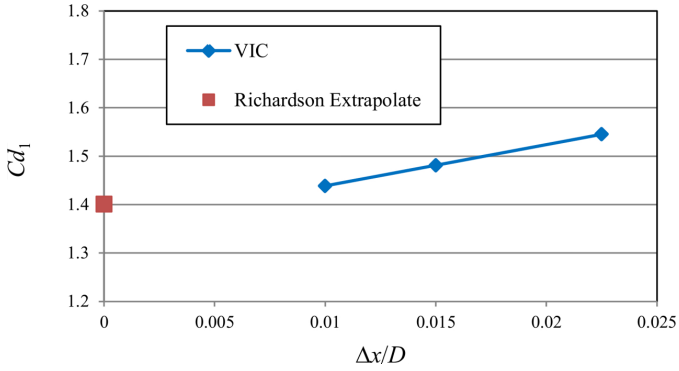

Fig. 4. Drag coefficient of the upper cylinder (Cd_1) at $U_0 t/(D/2) = 400$ in the simulation case of the flow around two side-by-side circular cylinders with their center distance of $L = 3D$ at Re = 200. The VIC method produces three values Cd_1s, and its value at the zero grid spacing is gained using the Richardson extrapolation method

The vortex wake pattern of flow around two side-by-side circular cylinders at Re in the range from 40 to 200 is investigated. Two cylinders are arranged in a vertical line normal to the upstream velocity, as shown in Fig. 2(b), their distance

(L) varies from $1.2D$ to $6D$, and the distance center is at the origin of the coordinate system. The reason for choosing this distance range is that whole flow patterns can occur, and the wake interference effects are negligible for a distance larger than $6D$. Moreover, we will discuss simulation results at several specific distances to represent others with the same flow wake characteristics. The drag and lift of the flow acting these cylinders are computed using two control volumes surrounding them. The computational domain, the grid spacing, and time step set up for these simulation cases are referred from the previous work [14].

3.1. Flow at Re = 40

The flow around two cylinders in the side-by-side arrangement at Re = 40 is first simulated. The computational domain of $(-7D, 68D) \times (-7.5D, 7.5D)$ is divided into 3750×750 grid nodes, and the computational time step $U_0\Delta t/(D/2)$ is set as 0.00125. Fig. 5 shows the instantaneous vorticity distribution of flow around two cylinders in the side-by-side arrangement at Re = 40 at $U_0 t/(D/2) = 400$. At the distance of $L = 1.5D$, the boundary layer separates from the cylinder surfaces, and the separation occurs at a certain point. The separation of flow forms shear layers on both sides of the cylinders. These shear layers at the distance side of both cylinders, called inner shear layers, are too weak to interact with the shear layers at the free-stream side, called outer shear layers, leading to complete suppression of the inner shear layers. In addition, the outer shear layers are not strong enough to roll up to form the vortices but elongate uninterrupted by the inner shear layers.

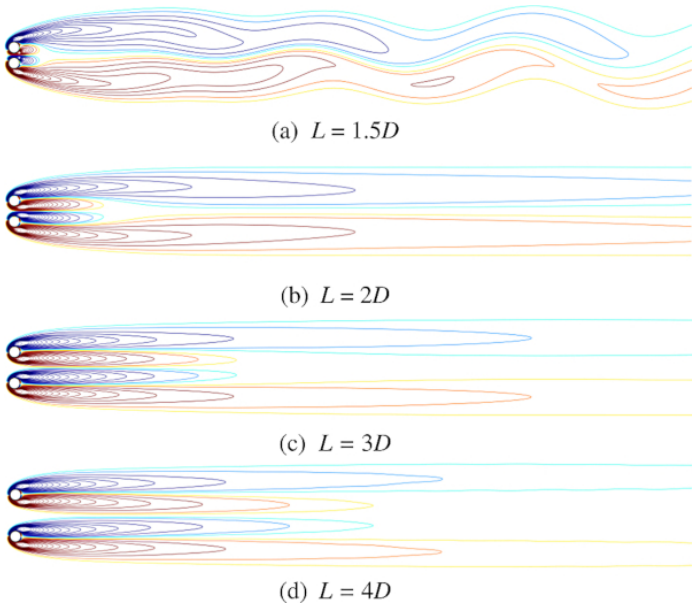

Fig. 5. Instantaneous vorticity distribution of the flow around two side-by-side cylinders at Re = 40 with their various distances (a) $L = 1.5D$, (b) $L = 2D$, (c) $L = 3D$, and (d) $L = 4D$

Subsequently, the outer shear layers deflect and behave in the meandering motion. This wake pattern is called the *meandering-motion*. This flow phenomenon is also observed in the evolution of the bubble plume rising freely from an annular cylinder placed in water, owing to the buoyancy effects [30]. The interaction of these shear layers detached from the cylinders decreases along with their distance, as illustrated in Fig. 5(b), Fig. 5(c), and Fig. 5(d). For the distances of $L = 2D, 3D$ and $4D$, the wake patterns are steady and symmetric regarding the horizontal axis. This flow wake pattern is named as *steady*.

Fig. 6 describes the time variation of drag and lift coefficients exerted on two side-by-side cylinders at Re = 40. The drag coefficients of the cylinders overlap. This is explained as the flow field behavior in regions near cylinders is steady; even two wake patterns exist at this Re. Values of the time-averaged lift coefficients of upper and lower cylinders are negative and positive. The mean repulsive force phenomenon is observed between two cylinders. This repulsiveness almost collapses at the distance of $L = 4D$, as displayed in Fig. 6(d). The interaction between two vortex wakes generated from the cylinders is negligible at this distance.

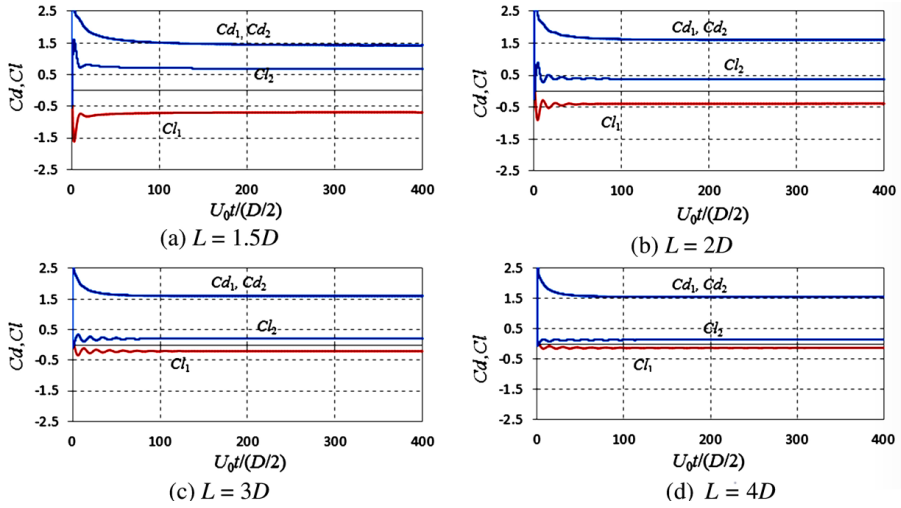

Fig. 6. Time variation of drag (Cd) and lift (Cl) coefficients exerted on two side-by-side cylinders at Re = 40, where subscripts 1 and 2 indicate the upper and lower cylinders, respectively. Cylinder distances are (a) $L = 1.5D$, (b) $L = 2D$, (c) $L = 3D$, and (d) $L = 4D$

3.2. Flow at Re = 100

Characteristics of the flow around two side-by-side cylinders at Re = 100 are investigated. The distance L between the cylinders is varied in the range from $1.5D$ to $4D$. A computation domain of $(-7D, 68D) \times (-7.5D, 7.5D)$ is divided into 5000×1000 grid nodes, and the computational time step $U_0\Delta t/(D/2)$ is set as 0.00125. Fig. 7 describes the instantaneous vorticity distribution around two

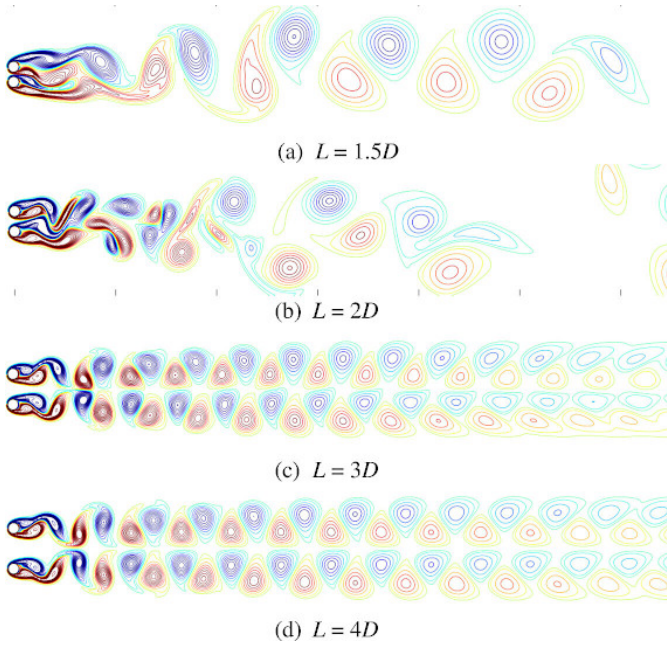

Fig. 7. Instantaneous vorticity distribution of the flow around two side-by-side cylinders at Re = 100 with their various distances (a) $L = 1.5D$, (b) $L = 2D$, (c) $L = 3D$, and (d) $L = 4D$

cylinders in the side-by-side arrangement at Re = 100 at $U_0t/(D/2) = 400$. At the small distance of $L = 1.5D$, the interaction of shear layers separated from cylinders prioritizes the inner ones. The inner shear layer of the upper cylinder deflects toward the lower cylinder and does not deflect back. This shear layer presses the inner shear layers of the lower cylinders. Consequently, this wake pattern comprises two wake structures with a wide near-wake behind the upper cylinder and a narrow near-wake behind the lower one. Note that the wide and narrow near-wakes express a part of the wake behind near the cylinder with large and narrow sizes in the vertical direction, respectively. Each near-wake is composed of two shear layers separated from a cylinder. The inner shear layer separated from the upper cylinder seems to make an effort in order to escape the confines of the outer shear layers detached from both cylinders. However, it is pulled back and weakened by the inner shear layer separated by the lower cylinder. The outer shear layers interact and generate vortices alternately to form a vortex wake similar to the Karman vortex street induced by the flow around a single bluff body. Moreover, the position of the wide near-wake and the narrow near-wake remains unchanged in the whole time evolution of the flow, as further explained using plots of Cd and Cl exerted on the cylinders later. This wake pattern is called *deflected-in-one-direction*.

At a larger distance of $L = 2D$, the inner shear layer from the upper cylinder deflects toward the lower cylinder, generating a wide near-wake and a narrow near-wake kept in a time interval. After several vortex sheddings, the wide near-wake

and the narrow near-wake positions are switched. The generation of vortices from the narrow near-wake is more rapid than from the wide near-wake. These vortices are randomly intermixed to form a vortex wake not similar to the Karman vortex street. This flow wake pattern is called *flip-flopping*. This phenomenon has features as the shear layers separated from cylinders deflect to the right and the left equally due to the Coanda effects [1]. In this flow phenomenon, one inner shear layer is considered a fluid jet, while another plays a role as a convex solid surface, and the fluid jet tends to attach to this surface. Bearman and Wadcock [2] verified that this apparent unsteadiness flow wake pattern is an intrinsic property of flow and not affected by experimental conditions. Zdravkovich [3] described this flow pattern as the gap flow forms a jet biased towards the narrow wake. The biased jet flow can switch in the opposite direction at irregular time intervals. The flow is bistable, and the switch of the asymmetric flow pattern causes exciting amplitude oscillations. Kim and Durbin [5] explained that the flip-flopping could be a loss of stability of the symmetric mean flow as the cylinders are brought into proximity.

At large distances of $L = 3D$ and $4D$, the interaction of the inner shear layers is weak, and the shear layers from each cylinder generate vortices periodically. These vortices form two parallel anti-phase vortex streets. These two vortex streets are symmetric to the horizontal centerline and combine to construct a vortex wake named as *anti-phase-synchronization*. The vortex shape remains unchanged in this wake type without any distortion downstream far from the cylinders. The synchronization in this wake pattern will be further explained using plots of Cd and Cl acting on the cylinders below.

The characteristics of the flow patterns are clarified using the plots of the time variation of drag and lift coefficients exerted on cylinders, as shown in Fig. 8. At the distance of $L = 1.5D$, the *deflected-in-one-direction* phenomenon occurs;

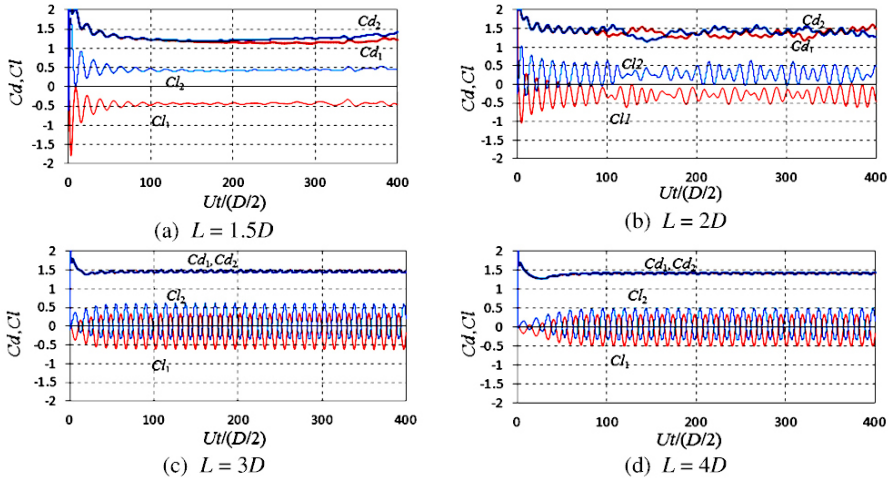

Fig. 8. Time variation of drag and lift coefficients exerted on two side-by-side cylinders at Re = 100 with their various distances (a) $L = 1.5D$, (b) $L = 2D$, (c) $L = 3D$, and (d) $L = 4D$

the drag coefficient of the lower cylinder is always higher than that of the upper one. This aspect explains the deflection in one direction of the inner shear layers generated from the upper cylinder toward the lower cylinder. The drag coefficient of the cylinder with the narrow near-wake is always higher than that with the wide near-wake. At the distance of $L = 2D$, the *flip-flopping* pattern is observed; the drag coefficient of the lower cylinder fluctuates around those of the upper cylinder. It is observed that the vortex structure with the wide near-wake behind the upper cylinder and the narrow near-wake behind the lower cylinder changes its direction after several vortex shedding. The lift coefficient of the cylinder with a higher drag coefficient fluctuates more rapidly than that of another cylinder with a lower one. In other words, the vortex shedding from the narrow near-wake is faster than that from the wide near-wake. At distances of $L = 3D$ and $4D$, the *anti-phase-synchronization* wake pattern takes place; the drag coefficients fluctuate in phase while the oscillation of lift coefficients is anti-phase. Moreover, the mean lift coefficients of cylinders for whole simulation cases are repulsive.

The vortex wake patterns of the flow around two side-by-side cylinders with their distances of $L = 2D$, $3D$, and $4D$ at Re = 100 under the disturbance effects on the initial flow condition during $3 \leqslant tU_0/(D/2) \leqslant 4$ are further investigated. The free-stream velocity during this period is set up as $\boldsymbol{u}_\infty = (U_0, \sin(2\pi t))$. Fig. 9 describes the instantaneous vorticity distribution of flow around two cylinders in the side-by-side arrangement at Re = 100 under the disturbance effects. At the distance of $L = 2$D, the *flip-flopping* wake pattern takes place, as observed in the simulation case without the disturbance effects shown in Fig. 7(b). This reconfirms the existence of the intrinsic instability of flow at a medium distance between cylinders. This flow pattern is not influenced by the external disturbance effects on the initial flow condition.

At the distance of $L = 3D$, the shear layers generated from cylinders roll up to form vortices alternately and establish two parallel in-phase vortex streets. These vortex streets are anti-symmetric regarding the horizontal axis, and they combine to form the *in-phase-synchronization* wake pattern. Vortex structures of this flow are only conserved in regions near the cylinders. The cancellation and coalescence of vortices to form large-scale vortices occur downstream at $20D$ from the cylinders. Williamson [4] described the pairing process of vortices that leads to the development of binary vortices. A binary vortex is a pair of like-signed vortices that rotate around one another. At the distance of $L = 4D$, there is a phase change of the vortex sheddings from two cylinders. A slight phase difference between vortex sheddings is observed at $tU_0/(D/2) = 200$, as shown by plots of Cl in Fig. 10(c). This difference causes an unequal collapse of two vortex streets behind the cylinders. The decay of the lower vortex street, generated from the lower cylinder, is more rapid than that of the upper vortex street from the upper one, as seen in Fig. 9(c). This vortex wake pattern of the flow is called *phase-difference-synchronization*. It gradually attains the *anti-phase-synchronization* one as time progresses, as shown in Fig. 9(d).

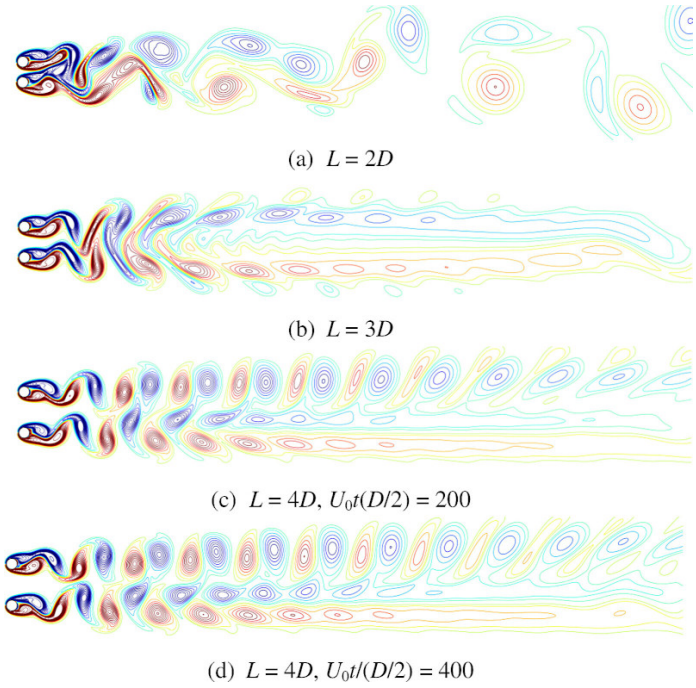

(a) $L = 2D$

(b) $L = 3D$

(c) $L = 4D$, $U_0t/(D/2) = 200$

(d) $L = 4D$, $U_0t/(D/2) = 400$

Fig. 9. Instantaneous vorticity distribution of the flow around two side-by-side cylinders at Re = 100 with their various distances (a) $L = 2D$, (b) $L = 3D$, (c) and (d) $L = 4D$, where the disturbance effects on the initial flow condition occur during $3 \leqslant tU_0/(D/2) \leqslant 4$

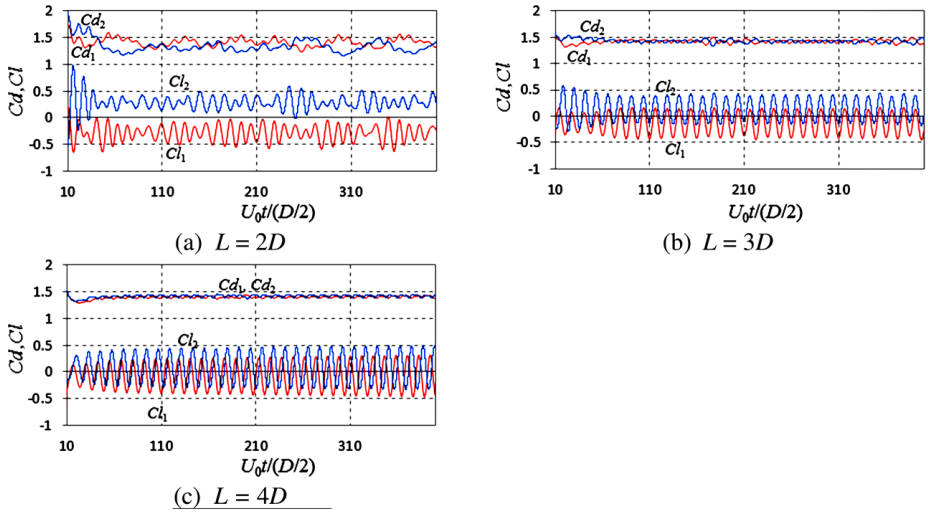

(a) $L = 2D$

(b) $L = 3D$

(c) $L = 4D$

Fig. 10. Time variation of drag and lift coefficients exerted on two side-by-side cylinders at Re = 100 with their various distances (a) $L = 2D$, (b) $L = 3D$, and (c) $L = 4D$, where the disturbance effects on the initial flow condition take place during $3 \leqslant tU_0/(D/2) \leqslant 4$

The time variation of drag and lift coefficients exerted on the cylinders, as illustrated in Fig. 10, further clarifies the characteristics of the flow pattern under the disturbance effects on the initial flow condition. At the distance of $L = 2D$, force coefficients of cylinders behave the same as those in the case of the flow around two cylinders without the disturbance effects, as seen in Fig. 8(b). At the distance of $L = 3D$, the fluctuations of lift coefficients of cylinders are *in-phase-synchronization*. Meanwhile, at the distance of $L = 4D$, the *phase-difference-synchronization* behavior of lift coefficients of cylinders develops from $tU_0/(D/2) = 10$ to 410. The flow pattern at the distance of $L = 4D$ is predicted to approach the *anti-phase-synchronization* pattern as time advances.

3.3. Flow at Re = 200

At Re = 200, the computational domain of $(-7D, 68D) \times (-7.5D, 7.5D)$ is divided into 7500×1500 grid nodes, and the time step $(U_0\Delta t/(D/2))$ is set as 0.00125. Fig. 11 describes the instantaneous vorticity distribution of flow around two cylinders at Re = 200. At the distance of $L = 1.2D$, the shear layers are shed on both sides of the cylinders. The inner shear layers seem to be confined to a closed dynamic region constructed by the outer shear layers, leading to the formation of vortices only from the outer shears. These shear layers roll up to create vortices and form the *single-bluff-body* wake pattern similar to a distorted Karman vortex street.

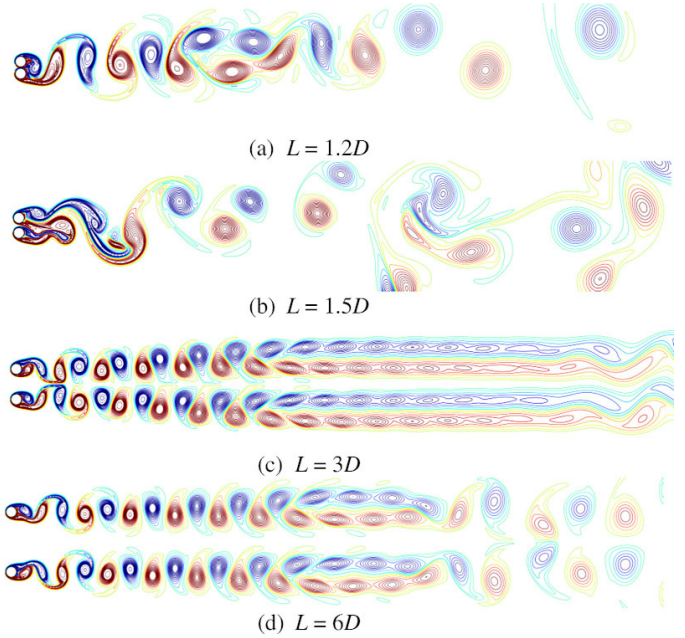

Fig. 11. Instantaneous vorticity distribution of the flow around two side-by-side cylinders at Re = 200 with their various distances (a) $L = 1.2D$, (b) $L = 1.5D$, (c) $L = 3D$, and (d) $L = 6D$

At the distance of $L = 1.5D$, the *flip-flopping* wake pattern takes place, as observed in the case of flow with $L = 2D$ at Re = 100. The flow pattern, including the wide near-wake and the narrow near-wake, deflects from one side to another and vice versa. At distances of $L = 3D$ and $6D$, the *anti-phase-synchronization* wake pattern is produced, and this pattern is symmetric with respect to the horizontal line. The shape of vortex structures is not conserved for the whole downstream, and these vortices are deformed and decay downstream at $40D$ from the cylinders.

The drag and lift coefficients acting on the cylinders are illustrated in Fig. 12. At the distance of $L = 1.2D$, the *single-bluff-body* wake pattern occurs; the fluctuations of lift coefficients are in phase, while those of drag coefficients are phase-difference. This is interpreted by the fact that the shear layers are separated from the free-stream side in-phase and form vortices periodically. In addition, the outer shear layers interact with inner shear layers to create closed dynamic regions. The effects of these regions result in a sharp fluctuation and an increase in the magnitude of the drag and lift coefficients, as observed in plots of Cd and Cl in Fig. 12(a). At the distance of $L = 1.5D$, the *flip-flopping* phenomena take place, and the drag and lift coefficients of cylinders behave as the same as that in the case of the flow with $L = 2D$ at Re = 100, where the Cd of the upper cylinder fluctuates around the Cd of the lower cylinder. This flow pattern excites both cylinders' oscillation amplitude of Cd and Cl. At distances of $L = 3D$ and $6D$, the drag coefficients fluctuate in phase, while the lift coefficients oscillate in anti-phase. This explains that the *anti-phase-synchronization* wake pattern occurs at these distances. Furthermore, the mean repulsive force between the cylinders collapses at $L = 6D$, where the maximum values of the lift coefficients observed are the same as that in the case of the flow around a single cylinder. This indicates that the interaction of vortex shedding from the cylinders vanishes away at this cylinder distance.

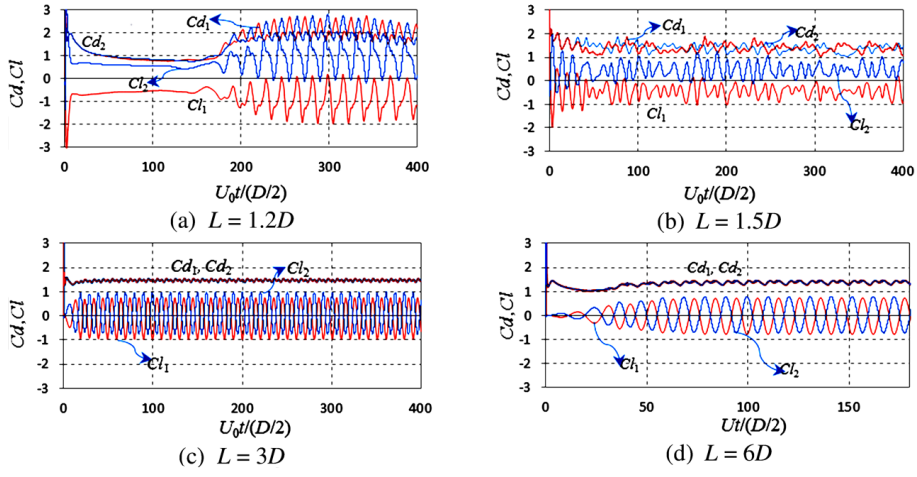

Fig. 12. Time variation of drag and lift coefficients exerted on two side-by-side cylinders at Re = 200 at their various distances (a) $L = 1.2D$, (b) $L = 1.5D$, (c) $L = 3D$, and (d) $L = 6D$

Fig. 13 describes the instantaneous vorticity distribution around two cylinders in the side-by-side arrangement at Re = 200 under the disturbance effects on the initial flow condition. The free-stream velocity during $3 \leq tU_0(D/2) \leq 4$ is set up as $\boldsymbol{u}_\infty = (U_0, \sin(2\pi t))$. At the distance of $L = 3D$, there is a change from the *phase-difference-synchronization* to the *anti-phase-synchronization* states of flow observed. This can be further seen in plots of the time variation of the drag and lift coefficients shown in Fig. 14(a). This phenomenon is explained as the interaction of two vortex streets in phase-difference during the initial stage deforms the shape of vortices near the region of the cylinders. These deformed vortices influence the separation of shear layers behind cylinders. The interaction between the deformed vortices and these shear layers leads to a delay in the phase-difference process. This delay results in recovering the symmetrical structure of the flow or the *anti-phase-synchronization* pattern. At the distance of $L = 4D$, the flow phenomenon is observed similar to $L = 3D$. However, the intensity of the interaction of two vortex streets significantly reduces, and the proportion of the vortex wake is recovered more rapidly than that at $L = 3D$, as further explained by plots of Cd and Cl later. At the distance of $L = 6D$, the flow wake pattern is *in-phase-synchronization* and remains unchanged from the beginning to the end of the flow evolution, as seen at $tU_0/(D/2) = 310$. There is no phase change observed at this cylinder distance. This can be explained as the vortex street generated from the upper cylinder is independent of the lower cylinder. The interaction intensity between these two vortex streets is trivial.

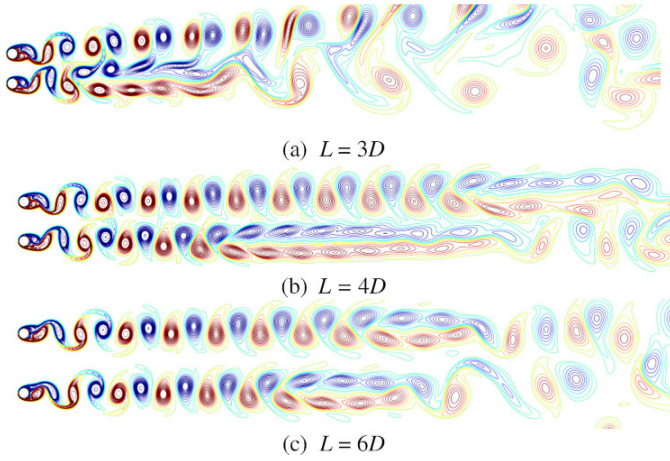

(a) $L = 3D$

(b) $L = 4D$

(c) $L = 6D$

Fig. 13. Instantaneous vorticity distribution of the flow around two side-by-side cylinders at Re = 200 with their various distances (a) $L = 3D$, (b) $L = 4D$, and (c) $L = 6D$. The disturbance effects in a short period of the flow on the vortex wake patterns are investigated

Fig. 14 shows the time variation of the drag and lift coefficients exerted on the cylinders, demonstrating the discussions in Fig. 13. At the distance of $L = 3D$, the *phase-difference-synchronization* state of lift coefficients of the cylinders is

observed during $10 \leqslant tU_0/(D/2) \leqslant 110$. The lift coefficients gradually approach the *anti-phase-synchronization* state as time processes. At the distance of $L = 4D$, the change from the *phase-difference-synchronization* to the *anti-phase-synchronization* states of lift coefficients of cylinders occurs rapidly, as seen in Fig. 14(b), due to a reduction in the interaction intensity of the vortex streets generated from two cylinders. At the distance of $L = 6D$, the lift coefficients of the cylinders are in phase during their whole time evolution, as seen in Fig. 14(c), because of the effects of the *anti-phase-synchronization* pattern.

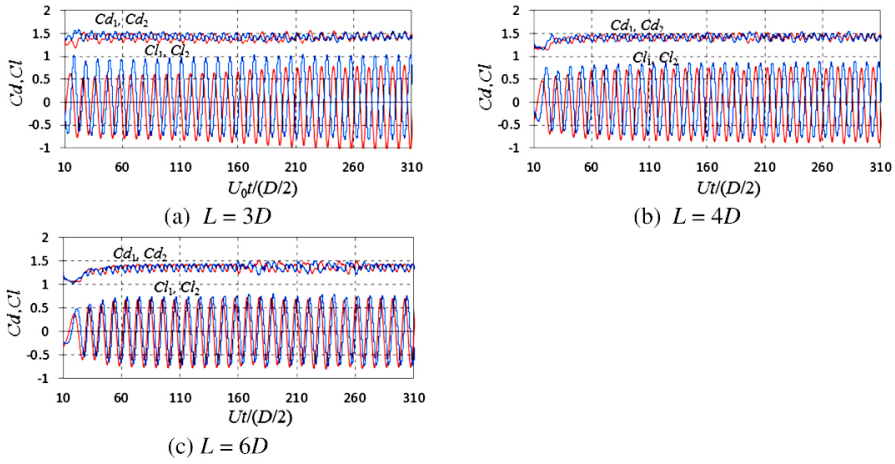

(a) $L = 3D$ (b) $L = 4D$

(c) $L = 6D$

Fig. 14. Time variation of drag and lift coefficients exerted on two side-by-side cylinders at Re = 200 with their various distances (a) $L = 3D$, (b) $L = 4D$, and (c) $L = 6D$, where the disturbance effects on the initial flow condition occur during $3 \leqslant tU_0(D/2) \leqslant 4$

Fig. 15 shows the instantaneous vorticity distribution around the cylinders at Re = 200, where the free-stream velocity during $3 \leqslant tU_0(D/2) \leqslant 4$ is set up as $\boldsymbol{u}_\infty = (\cos(2\pi t), \sin(2\pi t))$. The *in-phase-synchronization* pattern is observed at both distances of $L = 3D$ and $4D$, and this wake pattern does not change with time evolution. The shape of the same-signed vortices at the cylinder distance of $L = 3D$ is conserved until $8D$ downstream, while it is $20D$ for the distance of $L = 4D$. After the spacing from the cylinders ($8D$ and $20D$ corresponding to the cylinder distances of $L = 3D$ and $L = 4D$, respectively), the same-signed vortices merge to form large-scale vortices downstream. It is clear that the vortices in the *in-phase-synchronization* pattern are less stable than that in the *anti-phase-synchronization* one, as seen in Fig. 13.

Fig. 16 shows the time variation of the drag and lift coefficients exerted on two cylinders with their distances of $L = 3D$ and $4D$ at Re = 200. The fluctuation of drag coefficients of both cylinders is near in-phase, while that of the lift ones are in phase over the whole time of their evolution. These characteristics reconfirm the *in-phase-synchronization* pattern as observed above.

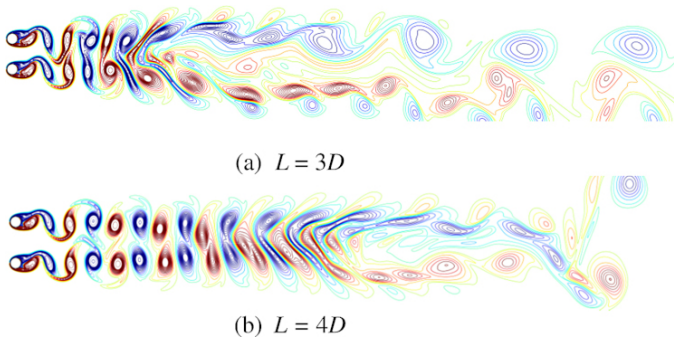

(a) $L = 3D$

(b) $L = 4D$

Fig. 15. Instantaneous vorticity distribution of the flow around two side-by-side cylinders at Re = 200 with their various distances (a) $L = 3D$ and (b) $L = 4D$, where the disturbance effects on the initial flow condition occur during $3 \leqslant tU_0(D/2) \leqslant 4$

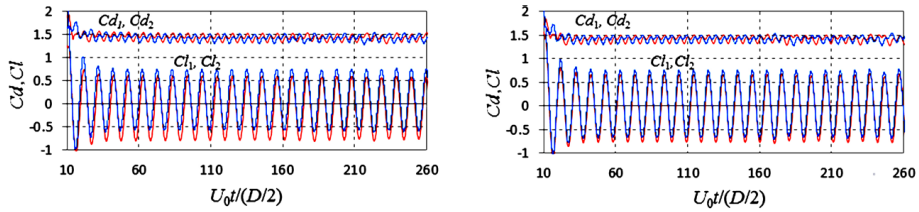

(a) $L = 3D$ (b) $L = 4D$

Fig. 16. Time variation of drag and lift coefficients exerted on two side-by-side cylinders at Re = 200 with their various distances (a) $L = 3D$ and (b) $L = 4D$, where the disturbance effects on the initial flow condition occur during $3 \leqslant tU_0(D/2) \leqslant 4$

4. Conclusions

The characteristics of flow around two side-by-side circular cylinders with their various distances varied from $1.2D$ to $6D$ at Re in the range from 40 to 200 are numerically investigated using a Vortex-in-cell method combined with a continuous-forcing immersed boundary method. The highlighted conclusions are given as follows:

1. The vortex wake of the flow is classified into eight patterns such as *single-bluff-body*, *steady*, *meandering-motion*, *deflected-in-one-direction*, *flip-flopping*, *anti-phase-synchronization*, *in-phase-synchronization*, and *phase-difference-synchronization*, significantly depending on the Re, the cylinder distance and the external disturbance effects on the initial flow conditions.
2. The *single-bluff-body* wake pattern develops at a small distance of the cylinders, and this distance decreases with the increase in Re. The vortex wake is similar to a distorted Karman vortex street, and the drag and lift coefficients acting on the cylinders significantly fluctuate.
3. The *steady* wake pattern is observed only at Re = 40. The vortices are not shed from the cylinders; instead, the shear layers at both sides elongate far

downstream. At this Re, when the cylinder distance is small, the *meandering-motion* wake pattern occurs. The shear layers also elongate downstream, and they behave in the meandering motion without vortices formed. Drag and lift coefficients exerted on the cylinders in two wake patterns do not fluctuate.

4. The *deflected-in-one-direction* wake pattern is observed at Re = 100 with a small distance between the cylinders. This vortex wake is composed of a wide near-wake and a narrow near-wake behind the cylinders, and the position of these wakes remains unchanged in their whole time evolution. Drag exerted on the cylinder with the narrow near-wake is always higher than those with the wide near-wake, and the vortices shed from the narrow near-wake are faster than that from the wide near-wake. The *flip-flopping* wake pattern occurs when the wide near-wake and the narrow near-wake are switched after several vortex sheddings. The distance between the cylinders for this wake pattern is medium, decreasing with Re. This flow wake pattern causes a great excitement in drag and lift coefficients.
5. The *anti-phase-* and *in-phase-synchronization* wake patterns are observed at a large cylinder distance. These flow patterns are composed of two Karman vortex streets in-phase and anti-phase. They can switch after a long time of the flow evolution. The flow in the *anti-phase-synchronization* pattern is more stable than that in the *in-phase-synchronization* one. The shapes of vortices in the *anti-phase-synchronization* pattern are conserved far downstream, while they are rapidly distorted with a certain spacing from the cylinders in the *in-phase-synchronization* pattern. The *phase-difference-synchronization* wake pattern can take place at a medium cylinder distance. This wake pattern tends to transform into the *anti-phase-synchronization* one. This transformation occurs slowly, forming two vortex streets asymmetrically behind the cylinders.
6. The mean repulsive force exists between the cylinder when they are brought into proximity, and the repulsiveness intensity reduces with the increase in the cylinder distance. At a significantly large distance between the cylinders, the near wakes generated are independent.

A. Grid convergence study by Richardson extrapolation method

A simulation produces a flow quantity $f(h)$ using a grid spacing h, the f at the zero grid spacing is considered to be the expected solution, f_{expected}. This expected value can be expressed in general form using the series expansion as follows:

$$f_{\text{expected}} = f(h) + Ch^p + C_1 h^{p+1} + C_2 h^{p+2} + \ldots \tag{21}$$

where p is the order of the error (order of convergence), and C, C_1 and C_2 are unknown constants. If h is small enough, $C_1 h^{p+1} + C_2 h^{p+2}$ is trivial compared to $f(h) + Ch^p$. Thus, Eq. (21) can be expressed as

$$f_{\text{expected}} = f(h) + Ch^p \,. \tag{22}$$

To investigate the order of convergence p, three values of f at three grid spacing h_1, h_2 and h_3 with their ratios r ($h_2 = rh_1$ and $h_3 = rh_2$) are employed as

$$f_{\text{expected}} = f(h_1) + Ch_1^p\,, \tag{23}$$

$$f_{\text{expected}} = f(h_2) + Ch_2^p\,, \tag{24}$$

$$f_{\text{expected}} = f(h_3) + Ch_3^p\,. \tag{25}$$

Subtracting both sides of Eq. (24) from those of Eq. (23) and those of Eq. (25) from Eq. (24), the resulting equations are taken the ratio, the order of convergence is derived as

$$p = \frac{\ln\left(\dfrac{f_3 - f_2}{f_2 - f_1}\right)}{\ln(r)}\,, \tag{26}$$

where $f_1 = f(h_1)$, $f_2 = f(h_2)$ and $f_3 = f(h_3)$. When subtracting both sides of Eq. (23) and Eq. (24) from f_1 and f_2, respectively, the results obtained are taken the ratio, and the expected value of f is expressed in the Richardson extrapolation term as

$$f_{\text{expected}} = f_1 + \frac{f_1 - f_2}{r^p - 1}\,. \tag{27}$$

References

[1] S. Ishigai, E. Nishikawa, K. Nishimura, and K. Cho. Experimental study on structure of gas flow in tube banks with tube axes normal to flow: Part 1, Karman vortex flow from two tubes at various spacings. *Bulletin of JSME*, 15(86):949–956, 1972. doi: 10.1299/jsme1958.15.949.

[2] P.W. Bearman and A.J. Wadcock. The interaction between a pair of circular cylinders normal to a stream. *Journal of Fluid Mechanics*, 61(3):499–511, 1973. doi: 10.1017/S0022112073000832.

[3] M.M. Zdravkovich. The effects of interference between circular cylinders in cross flow. *Journal of Fluids and Structures*, 1(2):239–261, 1987. doi: 10.1016/S0889-9746(87)90355-0.

[4] C.H.K. Williamson. Evolution of a single wake behind a pair of bluff bodies. *Journal of Fluid Mechanics*, 159:1–18, 1985. doi: 10.1017/S002211208500307X.

[5] H.J. Kim and P.A. Durbin. Investigation of the flow between a pair of circular cylinders in the flopping regime. *Journal of Fluid Mechanics*, 196:431–448, 1988. doi:10.1017/S0022112088002769.

[6] K.-S. Chang and C.-J.. Song. Interactive vortex shedding from a pair of circular cylinders in a transverse arrangement. *International Journal for Numerical Methods in Fluids*, 11(3):317–329, 1990. doi: 10.1002/fld.1650110305.

[7] S. Kang. Characteristics of flow over two circular cylinders in a side-by-side arrangement at low Reynolds numbers. *Physics of Fluids*, 15(9):2486, 2003. doi: 10.1063/1.1596412.

[8] A. Slaouti and P.K. Stansby. Flow around two circular cylinders by the random-vortex method. *Journal of Fluids and Structures*, 6(6):641–670, 1992. doi: 10.1016/0889-9746(92)90001-J.

[9] J.R. Meneghini, F. Saltara, C.L.R. Siqueira, and J.A. Ferrari Jr. Numerical simulation of flow interference between two circular cylinders in tandem and side-by-side arrangements. *Journal of Fluids and Structures*, 15(2):327–350, 2001. doi: 10.1006/jfls.2000.0343.

[10] W. Jester and Y. Kallinderis. Numerical study of incompressible flow about fixed cylinder pairs. *Journal of Fluids and Structures*, 17(4):561–577, 2003. doi: 10.1016/S0889-9746(02)00149-4.

[11] C.K. Birdsall and D. Fuss. Clouds-in-clouds, clouds-in-cells physics for many-body plasma simulation. *Journal of Computational Physics*, 3(4):494–511, 1969. doi: 10.1016/0021-9991(69)90058-8.

[12] I.P. Christiansen. Numerical simulation of hydrodynamics by the method of point vortices. *Journal of Computational Physics*, 13(3):363–379, 1973. doi: 10.1016/0021-9991(73)90042-9.

[13] G.-H. Cottet and P.D. Koumoutsakos. *Vortex Methods: Theory and Practice*. Cambridge University Press, 2000.

[14] V.L. Nguyen, R.Z. Lavi, and T. Uchiyama. Numerical simulation of flow around two tandem cylinders by vortex in cell method combined with immersed boundary method. *Advances and Applications in Fluid Mechanics*, 19(4):781–804, 2016. doi: 10.17654/FM019040787.

[15] V.L. Nguyen, T. Takamure, and T. Uchiyama. Deformation of a vortex ring caused by its impingement on a sphere. *Physics of Fluids*, 31(10):107108, 2019. doi: 10.1063/1.5122260.

[16] V. L. Nguyen, T. Nguyen-Thoi, and V. D. Duong. Characteristics of the flow around four cylinders of various shapes. *Ocean Engineering*, 238:109690, 2021.

[17] J.J. Monaghan. Extrapolating B splines for interpolation. *Journal of Computational Physics*, 60(2):253–262, 1985. doi: 10.1016/0021-9991(85)90006-3.

[18] J.H. Walther and P. Koumoutsakos. Three-dimensional vortex methods for particle-laden flows with two-way coupling. *Journal of Computational Physics*, 167(1):39–71, 2001. doi: 10.1006/jcph.2000.6656.

[19] C.S. Peskin. Flow patterns around heart valves: a numerical method. *Journal of Computational Physics*, 10(2):252–271, 1972. doi: 10.1016/0021-9991(72)90065-4.

[20] P. Angot, C.-H. Bruneau, and P. Fabrie. A penalization method to take into account obstacles in incompressible viscous flows. *Numerische Mathematik*, 81:497–520, 1999. doi: 10.1007/s002110050401.

[21] E.A. Fadlun, R. Verzicco, P. Orlandi, and J. Mohd-Yusof. Combined immersed-boundary finite-difference methods for three-dimensional complex flow simulations. *Journal of Computational Physics*, 191(1):35–60, 2000. doi: 10.1006/jcph.2000.6484.

[22] N.K.-R. Kevlahan and J.-M. Ghidaglia. Computation of turbulent flow past an array of cylinders using a spectral method with Brinkman penalization. *European Journal of Mechanics - B/Fluids*, 20(3):333–350, 2001. doi: 10.1016/S0997-7546(00)01121-3.

[23] M. Coquerelle and G.-H.Cottet. A vortex level set method for the two-way coupling of an incompressible fluid with colliding rigid bodies. *Journal of Computational Physics*, 227(21):9121–9137, 2008. doi: 10.1016/j.jcp.2008.03.041.

[24] F. Noca, D. Shiels, and D. Jeon. A comparison of methods for evaluating time-dependent fluid dynamic forces on bodies, using only velocity fields and their derivatives. *Journal of Fluids and Structures*, 13(5):551–578, 1999. doi: 10.1006/jfls.1999.0219.

[25] C. Mimeau, F. Gallizio, G.-H. Cottet, and I. Mortazavi. Vortex penalization method for bluff body flows. *International Journal for Numerical Methods in Fluids*, 79(2):55–83, 2015. doi: 10.1002/fld.4038.

[26] J.-I. Choi, R.C. Oberoi, J.R. Edwards, and J.A. Rosati. An immersed boundary method for complex incompressible flows. *Journal of Computational Physics*, 224(2):757–784, 2007. doi: 10.1016/j.jcp.2006.10.032.

[27] AB. Harichandan and A. Roy. Numerical investigation of low Reynolds number flow past two and three circular cylinders using unstructured grid CFR scheme. *International Journal of Heat and Fluid Flow*, 31(2):154–171, 2010. doi: 10.1016/j.ijheatfluidflow.2010.01.007.

[28] M. Braza, P. Chassaing, and H. Ha Minh. Numerical study and physical analysis of the pressure and velocity fields in the near wake of a circular cylinder. *Journal of Fluid Mechanics*, 165:79–130, 1986. doi: 10.1017/S0022112086003014.

[29] K. Supradeepan and A. Roy. Characterisation and analysis of flow over two side by side cylinders for different gaps at low Reynolds number: A numerical approach. *Physics of Fluids*, 26(6):063602, 2014. doi: 10.1063/1.4883484.

[30] V.L. Nguyen, T. Degawa, and T. Uchiyama. Numerical simulation of annular bubble plume by vortex in cell method. *International Journal of Numerical Methods for Heat and Fluid Flow*, 29(3):1103–1131, 2019. doi: 10.1108/HFF-03-2018-0094.